An Efficient Method for the Experimental Characterization of Periodic Multilayer Mirrors: A Global Optimization Approach

Mingfeng Li⬡, Said Mikki⬡, *Member, IEEE*, Paul C. Uzoma⬡, and Oleksiy V. Penkov⬡

Abstract— **This study proposes a new approach to periodic multilayer mirrors (PMMs) characterizations based on measured X-ray reflectivity (XRR) data. Here, XRR data are used to reconstruct the internal structure of PMMs using grazing incidence XRR (GIXR). A mathematical model of electromagnetic wave reflection by PMMs is employed to implement forward prediction, which will then be used iteratively in a global optimization framework in order to reconstruct the PMM unknown structure parameters. A typical simulation of PMM often includes tens to thousands of unknown structure parameters, rendering standard curve fitting methods cumbersome and impractical. To make the PMM characterization method computationally feasible, this study combines implementation of the Levy flight particle swarm optimization (LFPSO) algorithm with a parallelized version of the electromagnetic solver X-Ray Calc in order to simplify the model parameter reconstruction process. Levy flight, a random walk wherein the Levy distribution is used to determine step size, is a more efficient search strategy for global optimization because of the long jumps made by the particles. It is demonstrated that a PMM model with up to thousands of structure parameters can be reconstructed within several seconds on a regular workstation. The algorithm is tested with both measured and theoretical XRR data using in-house fabricated PMMs with known structures. Excellent agreement with the actual structures is observed, which is attained in short computation time. The new approach avoids manual curve fitting and simplified GIXR analysis and is observed to scale linearly with the size of the PMM structure, making it attractive for X-ray optics systems involving large-and-complex reflecting mirrors.**

Index Terms— **Grazing incidence X-ray reflectivity (GIXR), Levy flight particle swarm optimization (LFPSO), periodical multilayer mirrors.**

I. INTRODUCTION

X-RAY optics are used in various scientific and technological applications, such as X-ray photoelectron spectroscopy, free-electron lasers, X-ray astronomy [1], magnetic imaging [2], biomedical imaging, atomic physics [3], and new-generation lithography [4]. The performance of all these applications crucially relies on the reflectivity of periodic multilayer mirrors (PMMs) [5]. These PMM structures are coatings composed of tens or hundreds of alternating layers of "light" and "heavy" materials [6]. They are artificial Bragg crystals that reflect X-rays owing to constructive interference on periodically aligned interfaces. In particular, parameters such as interface roughness, layer thickness, density, and interlayer structure are used to define the overall structure of PMMs and predict their reflectivity [7], [8]. Reliable methods for characterizing PMM structures are therefore crucial for developing X-ray optics technology, which despite numerous advances is still a challenging active research topic [7], [9], [10].

Here, we focus on one particular approach, the grazing incidence X-ray reflectivity (GIXR) framework, which is a typical nondestructive PMMs characterization method. It is based on the analysis of characteristic reflectivity patterns in the area of grazing angles of $0°$–$5°$. The objective of our method is to feed measured X-ray reflectivity (XRR) data into a postprocessing module that would allow the user to reconstruct some or all the internal structural parameters of the PMM under X-ray illumination. However, this process, which is a nonlinear inverse problem, requires intensive calculations both in the forward and inverse problems. Indeed, the forward problem involves reflection and transmission of waves through multiple layers, a process that is essentially recursive and is sensitive to fine details such as wave polarization [11]. For the forward problem, the computation of XRR is based on Parratt's exact recursive method [12], while the inverse problem is the reconstruction of the multiple layers' structure based on XRR curve by using global optimization. Since Windt [13] presented one of the first XRR simulation software packages called IMD in 1998, other XRR computational tools have been developed, such as GenX [10], JGIXR [9], REFLEX [14], Multifitting [15], XOP [16], and X-Ray Calc [7]. In any case, all XRR parameters reconstruction (inverse scattering) processes that employ any of these methods in their forward iterative loop are similar in the sense of being computationally challenging ill-posed nonlinear inverse modeling problems. While this inverse problem is hard, it is necessary to automate the process of PMM structure parameters extraction using X-ray optics XRR measurement because manual curve fitting
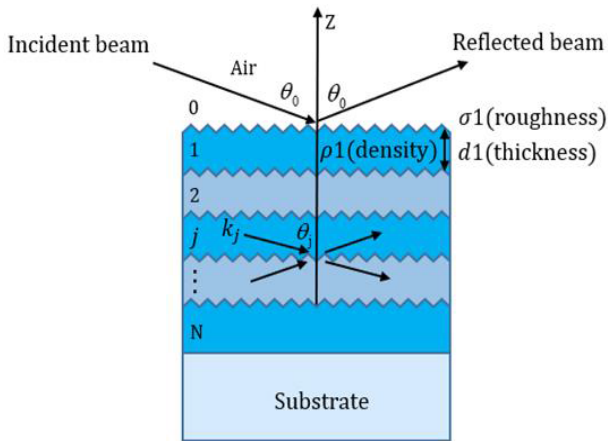
Fig. 1. Reflection and transmission of an incident beam ($\lambda = 1.54$ Å) from a PMM, j and k_j represent layer j and its wavevector, respectively.

becomes impractical with complex PMM configurations. In this article, we describe a possible such method with special emphasis on the ease of implementation and reduction of computational complexity.

For X-ray-optics-based PMM structure characterization methods, a PMM parameter structure model is first initiated, which includes the interface roughness, density, and interlayer thickness (see Fig. 1). Next, XRR data are simulated using a proper electromagnetic model and then compared with the XRR measurement within the framework of an iterative process. In every iteration, the parameters of the model are updated. The iterative process is considered complete when the discrepancy between the theoretical reconstructions of the electromagnetic model and the experimental data becomes minimal [17]. The fitting of the XRR curves of the PMMs can be simplified because the curves are periodic; therefore, the number of optimization parameters in the iterative process can be reduced. However, such parameter reduction is not always possible because the real structure cannot be exactly periodic. For example, unstable deposition conditions during the manufacturing process can cause deviations in layer thickness and interface roughness [8], [18], [19]. Hence, each layer is different and should be calculated independently. Interlayer mixing further complicates the structural model; in this case, a single stack in the PMM comprises two "primary layers" (light and heavy) and two other interface layers. Thus, the number of parameters described in a single stack is doubled. Therefore, if a stack comprises four layers, with each layer having three parameters (thickness, density, and roughness) and the PMMs having 300 or more stacks, a total of $4 \times 3 \times 300 = 3600$ parameters must be optimized. However, such an extremely high-dimensional optimization space requires a significant amount of user effort to manually refine the starting search guess for the optimization to converge in a reasonable time. Consequently, manual adjustment of thousands of parameters is impractical, and proper fitting cannot be realized.

As mentioned above, the optimization algorithms are a crucial part of the iteration process that are needed in order to minimize the discrepancy between theoretical reconstructions and experiment. Over the years, intelligent algorithms, such as differential evolution [10], genetic algorithms (GAs) [17], [20], and various swarm intelligent [9] algorithms, have been proposed for integration into software to solve various cumbersome inverse modeling problems. The least-square and gradient (hill-climbing) methods are unreliable owing to the stochastic search of the extremum in the solution domain. In contrast, intelligent algorithms combine the advantages of stochastic search with a smart solution-finding strategy, exhibiting better performance. However, without improvement, these intelligent algorithms are similar to classical algorithms and tend to converge prematurely [21], [22], resulting in the slow and unfavorable completion of a fitting. In addition, they are built-in software and fail to enhance their performance, typically requiring hours to complete a fitting.

There exists a large literature on solving this problem, which includes both specialized iterative algorithms [23], global optimization methods [24], and electromagnetic machine learning [25]. In this article, we follow the second path, where a recently developed variant of the global optimization method known as the Levy flight particle swarm optimization (LFPSO) [22], [26], [27] is integrated with a core electromagnetic model to solve the forward problem within an optimization-based iterative approach. Here, a mathematical model of the reflecting X-ray mirror is developed and exploited in order to compute the theoretical GIXR data based on any given PMM structure parameters. Afterward, an LFPSO is developed using an in-house code that is integrated with the electromagnetic solver. Based on the measured XRR data, an optimization cost function is formed and is used to train the direct (forward) electromagnetic model with the objective of predicting the optimum set of PMM structure parameters that yield a minimum curve-fitting cost function (lowest fitting error). Upon comparing the reconstructions of the theoretical model with the results of the optimization process, it is found that they fit well with experimental data.

This article is structured as follows. In Section II, we provide an outline of the electromagnetic model to be utilized for XRR calculations within the optimization process. The global optimization method itself is outlined in Section III. We choose particle swarm optimization (PSO) and concentrate on the recent modification known as Levy flight method LFPSO. In Section IV, we combine the forward model of Section II with the search algorithm of Section III in order to iteratively solve the inverse modeling (PMM structure characterization) problem (the code of LFPSO with X-Ray Calc is available online [28]). Finally, we end up with conclusion.

II. COMPUTATIONAL MODEL FOR XRR DATA

We first start by describing the method employed for computing the forward electromagnetic solution of the problem of X-ray wave scattering by PMMs, which is based here on the X-Ray Calc program. The computational framework X-Ray Calc is a fast and easy-to-use open access code available for simulating XRR in X-ray optics scenarios [7]. It was originally developed in order to simplify and facilitate structural parameters determination based on measured XRR and is equipped with a user-friendly interface.

The method implements a recursive computational procedure based on full-wave solution of Maxwell's equations [11] in order to estimate XRR data, while myriad dynamic scattering and absorption effects are also taken into consideration [7].

We briefly summarize the forward wave algorithm. First, the Fresnel equation [29] is used to calculate the reflectivity amplitude of the $(j + 1)$th interface through the fundamental electromagnetic reflection coefficient formula

$$r'_{j,j+1} = \frac{Q_j - Q_{j+1}}{Q_j + Q_{j+1}} \qquad (1)$$

$$Q_j = \begin{cases} (4\pi/\lambda)n_j\cos\theta_j, & s \text{ polarization} \\ (4\pi/\lambda n_j)\cos\theta_j, & p \text{ polarization} \end{cases} \qquad (2)$$

where λ, n_j, and θ_j are the radiation wavelength, complex refractive index of layer j, and propagation angle in layer j, respectively (see Fig. 1). The angle θ_j is obtained from the angle θ_0 in the incident medium of index n_0 using Snell's law $n_j\sin\theta_j = n_0\sin\theta_0$. It can be expressed as

$$\cos\theta_j = \sqrt{1 - \left(n_0/n_j\right)^2\sin^2\theta_0} \qquad (3)$$

where $n_j = 1 - \delta + i\beta$ is the refractive index of the jth layer, a complex number that depends on the wavelength. These may be estimated using the following formula [7]:

$$\binom{\delta}{\beta} = 0.54 \times 10^{-5}\frac{\rho}{\mu}\lambda^2\binom{f_1}{f_2} \qquad (4)$$

where ρ is the density of a layer (g/cm^3), μ is the atomic weight, λ is the wavelength (in Angstroms), and f_1 and f_2 are the real and complex parts of the atomic scattering factor, respectively [30].

The reflectivity coefficient for a multilayer structure with N layers as a function of the incidence angle is calculated recursively using the following relation:

$$r_{j-1,j} = \frac{r'_{j-1,j} + r_{j,j+1}e^{2i\varphi_j}}{1 + r'_{j-1,j}r_{j,j+1}e^{2i\varphi_j}} \qquad (5)$$

where i is the imaginary unit and $j = 0, 1, \ldots, N$. The ordered pair $(j - 1, j)$ represents the interface between the $(j - 1)$th and jth layers, and φ_j is the phase delay produced by the propagation of the wave through the jth layer, which depends on the total distance traveled and can be estimated as

$$\varphi_j = \frac{2\pi}{\lambda}d_j\cos\theta_j \qquad (6)$$

where d_j is the thickness of the jth layer (see Fig. 1).

The first step in the recursive algorithm involves calculating reflectivity from the interface between the bottom of the Nth layer and substrate. Since the bottommost substrate is presumed infinitely thick, there are no multiple reflections to consider there. Consequently, we have

$$r'_{N,\infty} = \frac{Q_N - Q_\infty}{Q_N + Q_\infty}. \qquad (7)$$

On the other hand, reflectivity from the top of the Nth layer is evaluated using (5), yielding

$$r_{N-1,N} = \frac{r'_{N-1,N} + r'_{N,\infty}e^{2i\varphi_N}}{1 + r'_{N-1,N}r'_{N,\infty}e^{2i\varphi_N}}. \qquad (8)$$

This process is repeated recursively until the total reflectivity amplitude $r_{0,1}$ at the interface between vacuum and the first layer is obtained. Subsequently, the reflectivity of the entire structure as a function of the illumination angle θ may be determined as $R(\theta) = |r_{0,1}|^2$. Finally, reflectivity losses caused by interface roughness or intermixture can be evaluated using the Debye–Waller-like correction factor [8]

$$R'_{j,j+1} = r'_{j,j+1}\exp\left(-\frac{16\pi^2\sigma_{j,j+1}^2\cos^2(\theta)}{\lambda^2}\right) \qquad (9)$$

where $\sigma_{j,j+1}$ is the effective interface thickness.

In order to form a proper optimization cost function, we need to measure how close is XRR simulation to the measured XRR data. Here, we utilize the χ^2 cost parameter, which quantifies the relation between reconstructed and experimental data. In our optimization scheme, this measure will be minimized and is expressed as

$$\chi^2 = \frac{1}{M}\sum_{i=1}^{M}\left(\frac{\log[R_{\exp}(\theta_i)] - \log[R_{\text{calc}}(\theta_i)]}{\log[R_{\exp}(\theta_i)]}\right)^2 \qquad (10)$$

where M denotes the total of measured (experimental) data points $R_{\exp}(\theta_i)$ in the range of incident angles from θ_0 to θ_M. Typically, M is in the range of 1000–4000. The theoretical value for a particular angle $R_{\text{calc}}(\theta_i)$ is obtained through relation (5).

Owing to the use of complex numbers for the description of the refraction coefficient and the large number of iterations that are typical for frequency-domain solutions of electromagnetic waves in multilayered structures such as PMMs [11], the simulation of an XRR curve, i.e., (1)–(10), as performed in the original X-Ray Calc code, is still computationally demanding even though the formulas are analytical. This is due to the recursive nature of the theory and the fact that typical X-ray mirrors are complex and involve many structural parameters. Moreover, in the iterative process of the global optimization algorithm to be used in this article (see Section III), for the search process to converge in a reasonable number of iterations, a very large number of cost function evaluations, i.e., computing (10) for all trial PMM structure parameters, must be attempted. Therefore, the computational cost of executing each iteration in the optimization process is very high and must be reduced. To accelerate the computation, the original X-Ray Calc code was modified as follows.

1) A parallel computation scheme was implemented, whereby the entire angular data range M was divided into n segments. Afterward, n is set equal to the number of central processing unit (CPU) cores available on the given computer platform.
2) A specialized in-house GUI-free implementation of the X-Ray Calc electromagnetic framework was developed. Avoiding GUI commands can accelerate the implementation of the overall scheme.

Consequently, the reflectivity in every segment is effectively computed in parallel, leading to an increase in the overall system computational speed almost linearly proportional to the number of available CPU cores. The use of a GUI-less application further improved the performance. For example,

the modified electromagnetic code could compute XRR curves for 20 different models within 0.2 s when launched on a regular six-core Intel CPU. To the best of our knowledge, such performance is superior to other tools stated previously. The parallelized in-house code performed batch processing of the PMM models and then generated and exported them to a data file for communication with the global optimization module described in Section III. After computing the χ^2 for every model in the batch, the PMM model with the lowest value of χ^2 was returned to our in-house code for further processing (optimization).

III. GLOBAL OPTIMIZATION FRAMEWORK (THE LFPSO ALGORITHM)

The crucial part of the X-ray-based PMM structure characterization method is the optimization algorithm, which is needed in order to find the proper structure parameters by minimizing the cost function χ^2 given by (10). In fact, it can be shown that this optimization cost function is highly nonlinear in terms of its optimization parameters. Therefore, efficient optimization methods such as the gradient descent method will not in general converge to the right solution unless the initial guess was already close to a global optimum. In fact, the cost function (10) suffers from the existence of multiple local minima, rendering the use of any local optimization algorithm challenging. On the other hand, standard heuristic optimization algorithms such as the GA require numerous fitness function calls (evaluations of the cost function), leading to high computational overhead per optimization iteration. For these reasons, we turn in this article toward using a global optimization method that is intermediate in complexity between the GA and the gradient descent method [31], [32].

PSO [33] is a population-based and resilient stochastic optimization approach originally inspired by the mobility and intelligence of swarms [34]. Several variations on the original PSO method have been proposed throughout the years and applied to numerous applications [27], [35], [36], [37], [38]. Due to its structural simplicity, robustness, ease of implementation, and convenient parameter settings, PSO has become very popular in engineering and science applications requiring cost-effective global optimization solution in a reasonable time. It is currently being used in various optimization problems, particularly for continuous objective functions and high-dimensional optimization problems [22].

We explain very briefly the key idea of the PSO framework, with focus on how the method is adapted to our X-ray-based PMM characterization method. Initially, all particles (solutions) are scattered randomly in the search space within preset bounds. Subsequently, the velocities and locations of the particles are updated during the computation step, and the particle velocity and location updates are computed as follows:

$$V_{i,d}^{t+1} = \omega V_{i,d}^t + c_1 \text{rand}_1(\text{pbest}_{i,d}^t - X_{i,d}^t)$$
$$+ c_2 \text{rand}_2(\text{gbest}_d^t - X_{i,d}^t) \quad (11)$$
$$X_{i,d}^{t+1} = X_{i,d}^t + V_{i,d}^{t+1} \quad (12)$$

where $V_{i,d}^{t+1}$ is the velocity of particle i at iteration $t + 1$ with respect to the dth dimension. Here, $X_{i,d}^t$ is the position

value of the ith particle with respect to the dth dimension. The parameter c_1 is the cognitive weighting factor, whereas c_2 is the social weighting factor. Furthermore, rand_1 and rand_2 are uniformly distributed random variables supplying the purely stochastic components of the algorithm, which are in the interval [0, 1]. The quantities pbest and gbest represent the best local positions for the current populations and the global best positions among particles, respectively. In addition, ω is the inertia weight, which is also added to PSO [35] to improve the global search ability of particles. According to [27], the adaptive formula of ω was chosen as follows:

$$\omega = 0.1 + 0.8 \left(1 - \frac{\text{iteration}}{T}\right) \quad (13)$$

where T denotes the total number of iterations to be used in the optimization process.

All unknown structural parameters of the PMM will be encoded into the particle's position. Let the ith particle (solution) describing the information of a PMM be denoted as

$$X_i = [H\sigma\rho] \quad (14)$$
$$X_u = [H_{ui} \ \sigma_{ui} \ \rho_{ui}] \quad (15)$$
$$X_l = [H_{li} \ \sigma_{li} \ \rho_{li}] \quad (16)$$

where H is a $1 \times Ll$ row vector representing the thickness, σ is a $1 \times Ll$ row vector representing the roughness, and ρ is a $1 \times Ll$ row vector representing the mass density. If a stack includes L layers and the PMMs consist of l stacks, the total number of parameters to be optimized is $L \times 3l$. For example, it was $4 \times 3 \times 300$ for the Mo/B PMMs described in [18]. Subsequently, the upper and lower bounds of (14) must be set, see (14) and (16), which constitutes the solution domain. Consequently, an m-sample set matrix can be defined as

$$X = [X_1, X_2, \ldots, X_m] \quad (17)$$

where m ($i \leq m$) denotes the number of particles (possible solutions) defined by users. Theoretically, the larger the number of particles, the better the fitting results. According to the results of our numerous trials, increasing the particle number will result in a longer fitting time but only a little improvement in the fitting effect. To ensure efficiency and good fitting results, we set m to 20. Naturally, users can also set larger parameter as necessary.

However, despite the simplicity of the basic PSO method with respect to other global optimization methods such as the GA, the PSO scheme continues to be too computationally demanding for the X-ray-based PMM structure determination problem considered in this article. This is mainly due to the very large optimization space associated with complex but still typical X-ray mirrors encountered in practice. To improve the PSO performance and further reduce the computational load, we deploy a very recent modification on the PSO algorithm known as the Levy flight framework. Levy flight algorithms are a new addition to the recently proposed PSO family [22], [27]. As shown in Fig. 2, the Levy flight is a variation on the theme of random walk based on executing Brownian motion with non-Gaussian randomly distributed step sizes of the distance traveled. As shown in Fig. 2, the axes represent
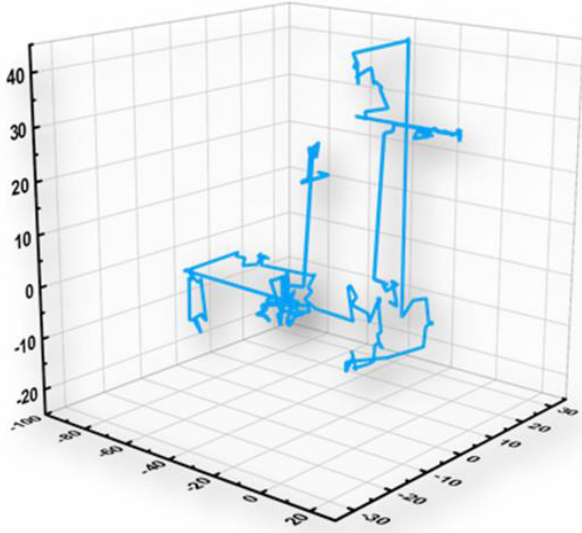
Fig. 2. Three-dimensional Levy flights of 200 sequential steps. The distance traveled in three dimension (thickness, roughness, and density) is indicated by the scale on the axe, and the scale on the axes represents the solution domain.

the search step size for each dimensional velocity separately. A negative value of velocity indicates that the reverse of the search motion. Levy flight method, see relation (18), is deployed as a strategy for updating the particle's velocity, resulting in the particle taking a long walk toward its local pbest and global gbest centers, hence increasing the swarm's variety and making it easier for the algorithm to execute global exploration throughout the search space. The dimensions represent the parameters (thickness, roughness, and density) for each layer. Here, we display a 3-D graphic. In unknown environments, Levy flight can increase the effectiveness and accuracy of PSO. In fact, such a modification may effectively prevent particles from falling into local optima [39].

According to (14), the search domain should be initialized to contain $L \times 3l$ Levy flights for each dimension. The relations (11) and (12) update the particle velocity and position with a probability greater than or equal to 0.5. However, if it is less than 0.5, the velocity of the particle is updated according to (18) and converted to its position as follows:

$$V_{i,d}^{t+1} = \omega \text{Levy\_walk}(X_{i,d}^t) + c_1 \text{rand}_1(\text{pbest}_{i,d}^t - X_{i,d}^t)$$
$$+ c_2 \text{rand}_2(\text{gbest}_d^t - X_{i,d}^t) \quad (18)$$
$$X_{i,d}^{t+1} = V_{i,d}^{t+1} \quad (19)$$
$$\text{Levy\_walk}(X_{i,d}^t)$$
$$= X_{i,d}^t + \Delta X \otimes Y \quad (20)$$

where Y is a vector with dimension equal to $X_{i,d}$ and elements as uniformly distributed random numbers in [0, 1]. The symbol $\otimes$ implies entrywise multiplication operation of two vectors. For the random walk's step size ΔX, this is given by

$$\Delta X = S \otimes X_{i,d}^t. \quad (21)$$

The step size S samples are given by

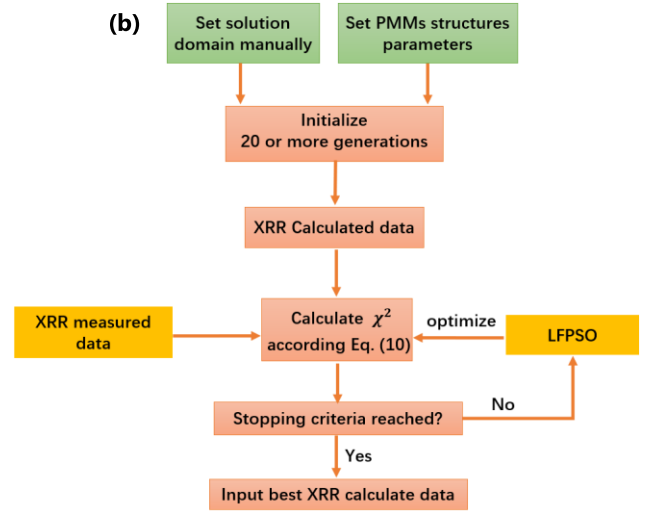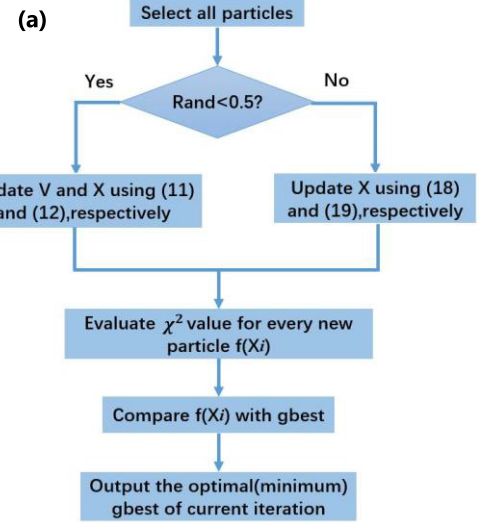$$S = 0.01 \frac{u}{|v|^{1/\beta}}(X_i^t - \text{gbest}^t) \quad (22)$$

Fig. 3. (a) Flowchart of the main XRR-based PMM characterization algorithm. (b) Flowchart of the LFPSO algorithm.

where β is the Levy distribution index, bounded as (0, 2]. Here $\beta = 1.5$; u and v are drawn from normal distributions

$$u \sim N(0, \sigma_u^2) v \sim N(0, \sigma_v^2) \quad (23)$$

with

$$\sigma_u = \left\{ \frac{\Gamma(1+\beta)\sin(\pi\beta/2)}{\Gamma[(1+\beta)/2]\beta 2^{(\beta-1)/2}} \right\}^{1/\beta}, \quad \sigma_v = 1 \quad (24)$$

where Γ is the standard gamma function. Fig. 3 shows the workflow of the LFPSO algorithm.

IV. IMPLEMENTATION AND VERIFICATION

The proposed XRR-based PMM structure determination method was implemented in an in-house code, and real-life measurement of XRR data of several PMMs fabricated in our laboratory was carried out. The accuracy of the LFPSO algorithm was verified by the reconstruction of the known PMMs structures. For this, several theoretical PMMs models were created in X-Ray Calc software and their
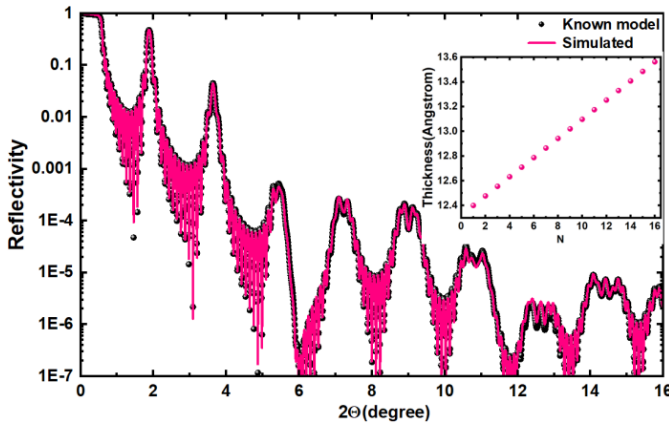
Fig. 4.   Example of XRR-based PMM characterization applied to XRR data generated by X-Ray Calc (dark dots). The model consisted of $16 \times$ B/MoB$_2$/Mo/MoB$_2$ stacks (192 optimization variables in total); Mo thickness was changed gradually as shown in the inset.

TABLE I

STACK-TO-STACK VARIATION OF MO LAYER THICKNESS (FIG. 4); h IS THE THICKNESS IN THE KNOWN MODEL; h^* IS THE THICKNESS RECONSTRUCTED BY LFPSO. THE ERROR IS CALCULATED BY $|h-h^*|/h$

N	H (Å)	H^* (Å)	Error (%)
1	12.42	12.40	0.160
2	12.49	12.47	0.161
3	12.55	12.53	0.198
4	12.63	12.60	0.250
5	12.71	12.70	0.149
6	12.78	12.78	0.106
7	12.86	12.89	0.241
8	12.94	12.93	0.173
9	13.02	13.02	0.138
10	13.09	13.07	0.152
11	13.18	13.17	0.106
12	13.26	13.25	0.134
13	13.33	13.31	0.134
14	13.40	13.39	0.137
15	13.48	13.46	0.144
16	13.56	13.59	0.243

XRR was simulated. Then, these simulated XRR dates were used as an input to reconstruct these theoretical models using the LFPSO method. The latter calls the X-Ray Calc electromagnetic source core iteratively within the global optimization process. Subsequently, optimum PMM model's structure parameters were obtained when the LFPSO algorithm converged. For all examples involving the LFPSO algorithm, a swarm population of a total of 20 particles (see relation 17) was considered, while the number of iterations was set to 20. The last choice of the number of iterations was dictated by trial-and-error method and was found to be sufficient to allow the reconstruction algorithm to accurately reconstruct the PMM structure parameters. The user can also set iterations lager if necessary. Silicon was used as the substrate for all the PMMs models, and all the XRR data were calculated for s-polarization. Initial models included several structural "defects" such as gradual change of layer thickness.

Fig. 4 shows the XRR data for the Mo/B PMM with a linear gradient of Mo generated by X-Ray Calc. Fig. 4 (inset) shows the distribution of the Mo thickness in the model as a function of the stack number. Here, the time required to complete the automatic reconstruction of the structure parameters using our parallelized LFPSO method was only 13.6 s for six cores Intel CPU without graphics processing unit (GPU) acceleration while using MATLAB R2021b. The data collected in Table I demonstrate that the thicknesses parameters reconstructed using our method are close to the actual parameters of the original PMM under X-ray illumination. In the next stage, PMM characterization algorithm was applied to XRR data generated using our theoretical electromagnetic model (X-Ray Calc) in order to evaluate the feasibility of applying our method to more complex models. The PMMs considered had 50, 100, and 300 stacks (see Fig. 5). In addition to the excellent PMM structure parameters results reported here, a nearly linear relationship between the elapsed time and increasing number of layers was observed, which suggests that even if the structure becomes more complicated, the model parameters reconstruction time will not scale up exponentially.
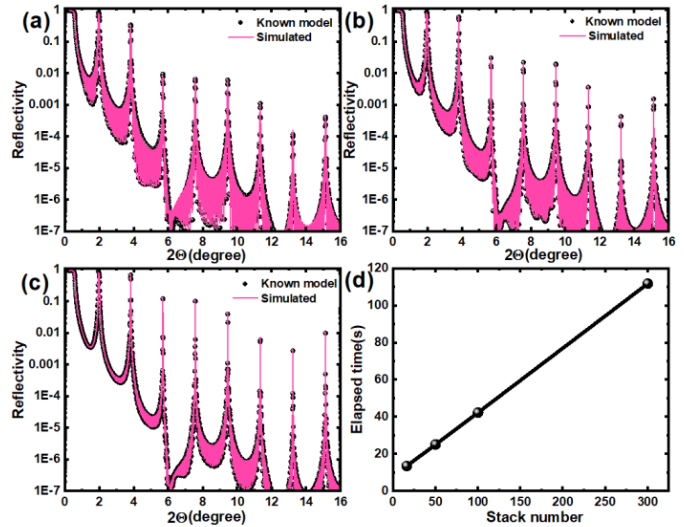

Fig. 5.   Example of applying our PMM characterization method to XRR data generated by X-Ray Calc (dark dots) for B/MoB$_2$/Mo/MoB$_2$ PMMs. Initial models had (a) 50, (b) 100, and (c) 300 stacks. (d) Structure model reconstruction time as a function of the number of stacks in a model.

We also provide an example with real-life measurement setup. The manufacturing of PMMs is performed by magnetron sputtering in the vacuum. The schematic of the deposition system is shown in Fig. 6(d) and (e). The deposition system mainly consists of magnetrons mounted on the top. A–C targets are installed on the magnetrons. A substrate holder is mounted below the magnetrons and is moved from one magnetron to another by a whirling arm to deposit alternate layers of A–C. A shutter with a circular window is used to control the deposition time. Fig. 6(c) shows the high resolution
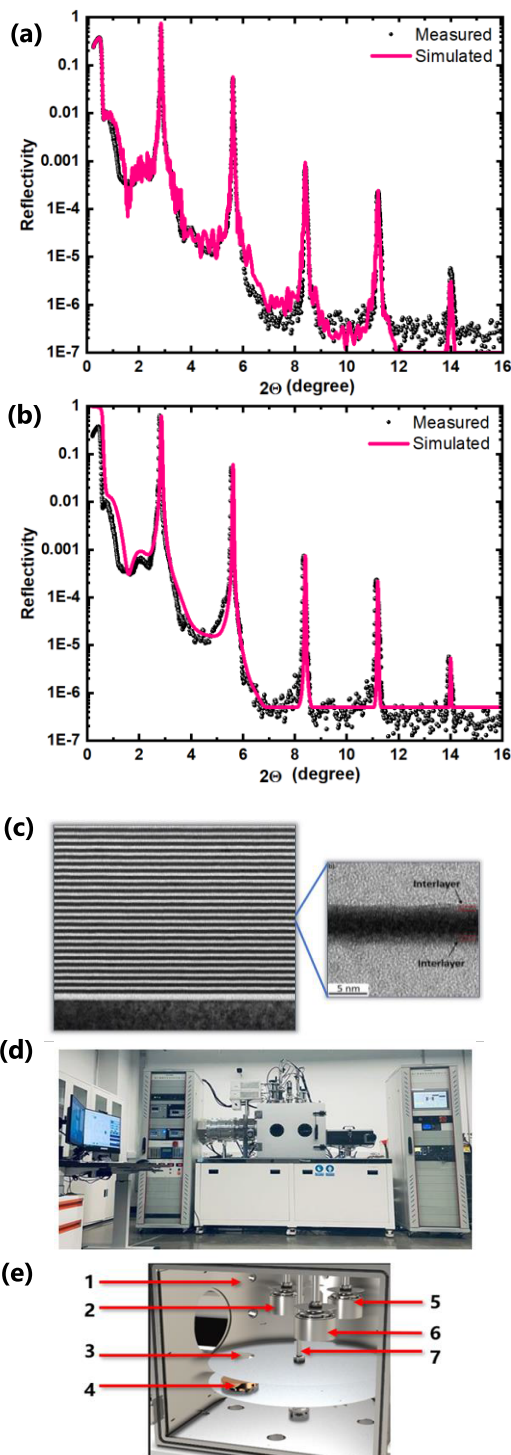
Fig. 6. (a) Automatic model reconstruction for measured PMMs model consisting of $300 \times$ B/MoB$_2$/Mo/MoB$_2$ multilayer, $\chi^2 = 0.0288$. (b) Manual fitting for measured PMMs model consisting of $300 \times$ B/MoB$_2$/Mo/MoB$_2$ multilayer (3600 optimization variables in total) [18], $\chi^2 = 0.0382$. (c) Cross-sectional HRTEM image of PMM [13]. (d) Image of the laboratory setup used for the deposition system. (e) Schematics of the deposition system for manufacturing PMMs. 1: Vacuum chamber, 2: magnetrons A, 3: shutter's circular window, 4: substrate holder, 5 and 6: magnetrons B and C, and 7: whirling arm.

transmission electron microscopy (HRTEM) image of the PMM. The measured XRR data of the real Mo/B PMMs were reconstructed using our method, and the first PMMs had 300 stacks; their structure is described elsewhere [18].
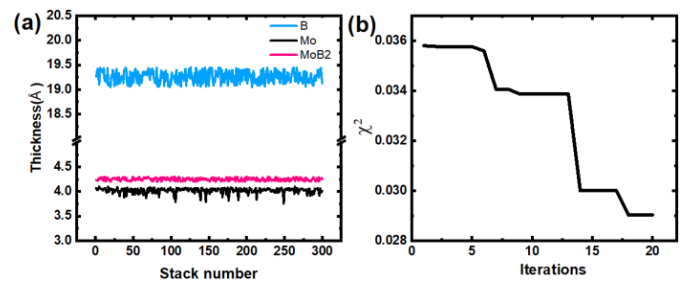

Fig. 7. Details for model reconstruction at Fig. 6(a). (a) Thickness distribution of all layers. (b) Minimum chi-square χ^2 [see (10)] during each iteration.
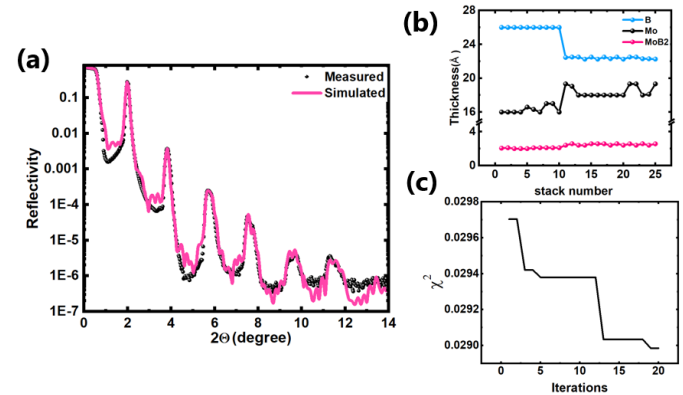

Fig. 8. (a) Result of model reconstruction by the new method of measured XRR curve for Mo/B PMMs consisting of 25 stacks (400 optimization variables in total) and having large thickness nonuniformity. (b) Thickness distribution of all layers. (c) Minimum chi-square χ^2 (10) error during every iteration.

The reconstruction results using the LFPSO method are shown in Fig. 6(a). The results in Fig. 7(a) reveal that the sputtering was not stable, resulting in the fluctuations of the thickness of the Mo and B layers owing to variations in the deposition rate [40]. Moreover, such fluctuations caused the broadening of diffraction peaks in the XRR curves. For comparison, Fig. 6(b) shows the result of the original "manual" PMM structure determination. It was obtained using the conventional approach, wherein the parameters of the stack were assumed constants, such that only a dozen parameters within a period (stack) were fitted in order to simplify the tedious manual process. However, this rarely results in the correct PMM structure parameters owing to the thickness drift. Certain software, such as IMD, employs an original GA to achieve automated fitting, which usually requires several hours and is inefficient because of the undesirable performance of the original GA.

For the model reconstruction shown in Fig. 6(a), 20 particles were initialized, and the number of iterations was set to 20; the elapsed time was only 101.9 s for the running environment described above, which is a greater speed than that in [17]. Tiilikainen et al. [17] described 15 periods, each consisting of three layers; however, the elapsed time was approximately 1600 s. One of the advantages of the new method proposed here and that in [17] is the integration of the calculation of the time-consuming recursive reflectivity formulas into the executable file (X-Ray Calc), which in our case calculates

the cost function (10) in only about 0.008 s in a system utilizing six cores Intel CPU. In addition, the LFPSO algorithm was reported to be superior to the GA algorithm in high-dimensional optimization problems [21], particularly for the fitting of PMMs. Once the period of the PMMs increases to several hundreds, the model reconstruction time in case of the GA would increase dramatically, whereas in our approach, it has been observed to maintain a linear growth relationship for the LFPSO. As shown in Fig. 6, the automatic PMM structure reconstruction result for LFPSO ($\chi^2 = 0.0288$) was better than that for manual fitting ($\chi^2 = 0.0382$). Furthermore, the peak and full-width at half-maximum (FWHM) fitted in Fig. 6(a) were superior to those fitted in Fig. 6(b), demonstrating the convenience of the new program for XRR-based model characterization.

As illustrated in Fig. 7(a), the thickness of each layer was obtained from GIXR, on the basis of which parametric information about undesirable compound MoB_2 and knowledge of the layer growth were also acquired. Owing to constant temperature conditions during deposition [18], the roughness of each interlayer was the same, just as the density of each layer. Fig. 7(b) shows that the cost function (10) decreases with an increase in the number of iterations, indicating convergence. If the reconstruction results are not satisfactory, then more than 20 particles can be initialized or more than 20 iterations can be set; however, the elapsed time will be prolonged. Fig. 8 illustrates the structure parameters reconstruction results for the Mo/B PMMs deposited without careful stabilization of the deposition conditions; significant deviations in the layer thickness were observed. In addition, the thickness of MoB_2 increased during deposition, revealing insufficient substrate cooling [18].

Finally, it is worth adding that users are free to modify the LFPSO algorithm in order to enhance optimization performance. For instance, LFPSO combines chaos [21], butterfly algorithm [41], and other intelligent algorithms in order to improve its performance. All structure parameters obtained from all layers can be used to further analyze the growth of the coatings, interlayer mixing, periodic drift, and other undesirable phenomena. Moreover, larger particles and iterations or narrowing of the solution domain can be specified to enhance the reconstruction accuracy; however, note that this last modification comes at the expense of execution longer time.

V. Conclusion

A new software package that combines the electromagnetic solution of reflectivity (X-Ray Calc) with global optimization (LFPSO) was developed to reconstruct unknown structure parameters of PMMs for X-ray optics applications. The proposed PMM characterization method resulted in a reliable global search and a high convergence rate inverse modeling algorithm, where many unknown structure parameters, mainly thickness, roughness, and densities were estimated based on measured XRR data. Rather than manually reconstructing thousands of parameters, simple operations such as importing experimental XRR data and setting up the solution

domain allowed the program to perform automatic PMM characterization in real time. The method was verified by comparison with measured and theoretical XRR data and excellent agreement between the technique's reconstructions and the actual PMM structure were observed. In addition, all parameters from all layers were obtained with knowledge of the details of layers growth, while significantly reducing the computational time compared with other global optimization methods such as GA. Since the number of layers in X-ray optical mirrors is expected to grow in the future with the development of new applications such as the next-generation extreme ultraviolet (EUV) lithography and other advanced X-ray imaging technologies, the proposed algorithm offers a robust and efficient addition to other currently used methods.

References

[1] C. R. Bower, K. L. Dietz, B. D. Ramsey, and M. C. Weisskopf, "Background in X-ray astronomy proportional counters," *IEEE Trans. Nucl. Sci.*, vol. 38, no. 2, pp. 585–590, Apr. 1991, doi: 10.1109/23.289361.

[2] P. Fischer, "X-ray imaging of magnetic structures," *IEEE Trans. Magn.*, vol. 51, no. 2, pp. 1–31, Feb. 2015, doi: 10.1109/TMAG.2014.2363054.

[3] J. Marton et al., "New X-ray detectors for exotic atom research," *IEEE Trans. Nucl. Sci.*, vol. 56, no. 3, pp. 1400–1404, Jun. 2009, doi: 10.1109/TNS.2008.2005980.

[4] P. C. Uzoma, S. Shabbir, H. Hu, P. C. Okonkwo, and O. V. Penkov, "Multilayer reflective coatings for BEUV lithography: A review," *Nanomaterials*, vol. 11, no. 11, p. 2782, Oct. 2021, doi: 10.3390/nano11112782.

[5] I. V. Kozhevnikov and A. V. Vinogradov, "Multilayer X-ray mirrors," *J. Russian Laser Res.*, vol. 16, no. 4, pp. 343–385, Jul. 1995, doi: 10.1007/BF02581074.

[6] E. Spiller, "14. Reflecting optics: Multilayers," in *Experimental Methods in the Physical Sciences*, vol. 31. Amsterdam, The Netherlands: Elsevier, 1998, pp. 271–288, doi: 10.1016/S0076-695X(08)60048-4.

[7] O. V. Penkov, I. A. Kopylets, M. Khadem, and T. Qin, "X-ray Calc: A software for the simulation of X-ray reflectivity," *SoftwareX*, vol. 12, Jul. 2020, Art. no. 100528, doi: 10.1016/j.softx.2020.100528.

[8] I. A. Makhotkin et al., "Short period La/B and LaN/B multilayer mirrors for similar to 6.8 nm wavelength," *Opt. Exp.*, vol. 21, no. 24, pp. 29894–29904, Dec. 2013, doi: 10.1364/oe.21.029894.

[9] D. Ingerle, G. Pepponi, F. Meirer, P. Wobrauschek, and C. Streli, "JGIXA—A software package for the calculation and fitting of grazing incidence X-ray fluorescence and X-ray reflectivity data for the characterization of nanometer-layers and ultra-shallow-implants," *Spectrochim. Acta B, At. Spectrosc.*, vol. 118, pp. 20–28, Apr. 2016, doi: 10.1016/j.sab.2016.02.010.

[10] M. Björck and G. Andersson, "GenX: An extensible X-ray reflectivity refinement program utilizing differential evolution," *J. Appl. Crystallogr.*, vol. 40, no. 6, pp. 1174–1178, Dec. 2007, doi: 10.1107/S0021889807045086.

[11] *Radiation and Scattering of Waves | IEEE eBooks | IEEE Xplore*. Accessed: Nov. 1, 2022. [Online]. Available: https://ieeexplore.ieee.org/book/5264502

[12] L. G. Parratt, "Surface studies of solids by total reflection of X-rays," *Phys. Rev.*, vol. 95, no. 2, pp. 359–369, Jul. 1954, doi: 10.1103/PhysRev.95.359.

[13] D. L. Windt, "IMD—Software for modeling the optical properties of multilayer films," *Comput. Phys.*, vol. 12, no. 4, p. 360, 1998, doi: 10.1063/1.168689.

[14] G. Vignaud and A. Gibaud, "REFLEX: A program for the analysis of specular X-ray and neutron reflectivity data," *J. Appl. Crystallogr.*, vol. 52, no. 1, pp. 201–213, Feb. 2019, doi: 10.1107/S1600576718018186.

[15] M. Svechnikov, "Multifitting: Software for the reflectometric reconstruction of multilayer nanofilms," *J. Appl. Crystallogr.*, vol. 53, no. 1, pp. 244–252, Feb. 2020, doi: 10.1107/S160057671901584X.

[16] M. S. del Río and R. J. Dejus, "XOP v2.4: Recent developments of the X-ray optics software toolkit," *Proc. SPIE*, vol. 8141, Sep. 2011, Art. no. 814115, doi: 10.1117/12.893911.

[17] J. Tiilikainen et al., "Genetic algorithm using independent component analysis in X-ray reflectivity curve fitting of periodic layer structures," *J. Phys. D, Appl. Phys.*, vol. 40, no. 19, pp. 6000–6004, Oct. 2007, doi: 10.1088/0022-3727/40/19/033.

[18] O. V. Penkov, I. A. Kopylets, V. V. Kondratenko, and M. Khadem, "Synthesis and structural analysis of Mo/B periodical multilayer X-ray mirrors for beyond extreme ultraviolet optics," *Mater. Des.*, vol. 198, Jan. 2021, Art. no. 109318, doi: 10.1016/j.matdes.2020.109318.

[19] S. Braun, H. Mai, M. Moss, R. Scholz, and A. Leson, "Mo/Si multilayers with different barrier layers for applications as extreme ultraviolet mirrors," *Jpn. J. Appl. Phys.*, vol. 41, pp. 4074–4081, Jun. 2002, doi: 10.1143/JJAP.41.4074.

[20] A. Ulyanenkov, K. Omote, and J. Harada, "The genetic algorithm: Refinement of X-ray reflectivity data from multilayers and thin films," *Phys. B, Condens. Matter*, vol. 283, nos. 1–3, pp. 237–241, Jun. 2000.

[21] B. Liu, L. Wang, Y.-H. Jin, F. Tang, and D. X. Huang, "Improved particle swarm optimization combined with chaos," *Chaos, Solitons Fractals*, vol. 25, no. 5, pp. 1261–1271, 2005, doi: 10.1016/j.chaos.2004.11.095.

[22] H. Haklı and H. Uğuz, "A novel particle swarm optimization algorithm with Lévy flight," *Appl. Soft Comput.*, vol. 23, pp. 333–345, Oct. 2014, doi: 10.1016/j.asoc.2014.06.034.

[23] D. Colton and R. Kress, *Inverse Acoustic and Electromagnetic Scattering Theory*, vol. 93. Cham, Switzerland: Springer, 2019, doi: 10.1007/978-3-030-30351-8.

[24] C. Xudong, N. Guangzheng, and Y. Shiyou, "An improved Tabu algorithm applied to global optimizations of inverse problems in electromagnetics," *IEEE Trans. Magn.*, vol. 38, no. 2, pp. 1069–1072, Mar. 2002, doi: 10.1109/20.996274.

[25] A. M. Alzahed, S. Mikki, and Y. Antar, "Electromagnetic machine learning for inverse modeling using the spatial singularity expansion method," *IEEE J. Multiscale Multiphys. Comput. Techn.*, vol. 5, pp. 59–71, 2020, doi: 10.1109/JMMCT.2020.2973101.

[26] A. H. Gandomi and A. R. Kashani, "Construction cost minimization of shallow foundation using recent swarm intelligence techniques," *IEEE Trans. Ind. Informat.*, vol. 14, no. 3, pp. 1099–1106, Mar. 2018, doi: 10.1109/TII.2017.2776132.

[27] R. Jensi and G. W. Jiji, "An enhanced particle swarm optimization with Lévy flight for global optimization," *Appl. Soft Comput.*, vol. 43, pp. 248–261, Jun. 2016, doi: 10.1016/j.asoc.2016.02.018.

[28] O. Penkov. (Jan. 30, 2023). *X-RayCalc*. Accessed: Feb. 8, 2023. [Online]. Available: https://github.com/OleksiyPenkov/X-RayCalc

[29] E. Spiller, *Soft X-Ray Optics*. Bellingham, WA, USA: SPIE, 1994.

[30] B. L. Henke, E. M. Gullikson, and J. C. Davis, "X-ray interactions: Photoabsorption, scattering, transmission, and reflection at $E = 50 - 30, 000 eV$, $Z = 1 - 92$," *At. Data Nucl. Data Tables*, vol. 54, p. 181, 1993, doi: 10.1006/adnd.1993.1013.

[31] V. Roberge, M. Tarbouchi, and G. Labonte, "Comparison of parallel genetic algorithm and particle swarm optimization for real-time UAV path planning," *IEEE Trans. Ind. Informat.*, vol. 9, no. 1, pp. 132–141, Feb. 2013, doi: 10.1109/TII.2012.2198665.

[32] K. E. Parsopoulos and M. N. Vrahatis, "On the computation of all global minimizers through particle swarm optimization," *IEEE Trans. Evol. Comput.*, vol. 8, no. 3, pp. 211–224, Jun. 2004, doi: 10.1109/TEVC.2004.826076.

[33] J. Kennedy and R. Eberhart, "Particle swarm optimization," in *Proc. Int. Conf. Neural Netw. (ICNN)*, Perth, WA, Australia, vol. 4, 1995, pp. 1942–1948, doi: 10.1109/ICNN.1995.488968.

[34] S. M. Mikki and A. A. Kishk, *Particle Swarm Optimization: A Physics-Based Approach*. Cham, Switzerland: Springer, 2008, doi: 10.1007/978-3-031-01704-9.

[35] Y. Shi and R. Eberhart, "A modified particle swarm optimizer," in *Proc. IEEE Int. Conf. Evol. Comput. IEEE World Congr. Comput. Intell.*, May 1998, pp. 69–73.

[36] S. M. Mikki and A. A. Kishk, "Hybrid periodic boundary condition for particle swarm optimization," *IEEE Trans. Antennas Propag.*, vol. 55, no. 11, pp. 3251–3256, Nov. 2007, doi: 10.1109/TAP.2007.908810.

[37] J. Persano, S. M. Mikki, and Y. M. M. Antar, "Gradient population optimization: A tensorflow-based heterogeneous non-von-Neumann paradigm for large-scale search," *IEEE Access*, vol. 6, pp. 77097–77122, 2018, doi: 10.1109/ACCESS.2018.2868236.

[38] Z.-H. Zhan, J. Zhang, Y. Li, and H. S.-H. Chung, "Adaptive particle swarm optimization," *IEEE Trans. Syst., Man, Cybern. B, Cybern.*, vol. 39, no. 6, pp. 1362–1381, Dec. 2009, doi: 10.1109/TSMCB.2009.2015956.

[39] E. H. Houssein, M. R. Saad, F. A. Hashim, H. Shaban, and M. Hassaballah, "Lévy flight distribution: A new Metaheuristic algorithm for solving engineering optimization problems," *Eng. Appl. Artif. Intell.*, vol. 94, Sep. 2020, Art. no. 103731, doi: 10.1016/j.engappai.2020.103731.

[40] C. Montcalm et al., "Survey of Ti-, B-, and Y-based soft x-ray-extreme ultraviolet multilayer mirrors for the 2- to 12-nm wavelength region," *Appl. Opt.*, vol. 35, no. 25, pp. 5134–5147, Sep. 1996, doi: 10.1364/ao.35.005134.

[41] M. Zhang, D. Long, T. Qin, and J. Yang, "A chaotic hybrid butterfly optimization algorithm with particle swarm optimization for high-dimensional optimization problems," *Symmetry*, vol. 12, no. 11, p. 1800, Oct. 2020, doi: 10.3390/sym12111800.